Supporting Information

Electrical and SERS detection of disulfide-mediated dimerization in single-molecule benzene-1,4-dithiol junctions

Jueting Zheng‡, Junyang Liu‡, Yijing Zhuo, Ruihao Li, Xi Jin, Yang Yang*, Zhao-Bin Chen, Jia Shi, Zongyuan Xiao, Wenjing Hong*, Zhong-qun Tian

State Key Laboratory of Physical Chemistry of Solid Surfaces, College of Chemistry and Chemical Engineering & Pen-Tung Sah Institute of Micro-Nano Science and Technology, Graphene Industry and Engineering Research Institute, iChEM, Xiamen University, Xiamen 361005, China

‡ These authors contributed equally.

Abstract: We applied a combined mechanically controllable break junction (MCBJ) and in-situ surface enhanced Raman spectroscopy (SERS) method to investigate the long-standing single-molecule conductance discrepancy of the prototypical benzene-1,4-dithiol (BDT) junctions. The single-molecule conductance characterization, together with the configuration analysis of the molecular junction suggested that the disulfide-mediated dimerization of BDT contributed to the low conductance feature, which was further verified by the detection of the S-S bond formation by in-situ SERS characterization. Control experiments demonstrated that the disulfide-mediated dimerization could be tuned via the chemical inhibitor. Our findings suggest that the combined electrical and SERS method is capable of probing chemical reaction at single-molecule level.

Table of Contents

1. Experimental details about the conductance measurements.

The benzene-1,4-dithiol (**BDT**, 97%) and pentane-1,5-dithiol (PDT, 98%) were purchased from Alfa Aesar. Tris(2-carboxyethyl)phosphine Hydrochloride (TCEP) was purchased from Tokyo Chemical Industry (TCI). Ethanol (EtOH) and 1, 3, 5-trimethylbenzene (TMB) were purchased from Sigma-Aldrich and all reagents were used without further purification.

We performed the blank experiment prior to the electrical characterization of **BDT**. Particularly, the clean gold electrodes pair, which were immersed in a mixed ethanol (EtOH) and 1, 3, 5-trimethylbenzene (TMB) solvent (EtOH/TMB =1:49, *v*/*v*), were opened and closed repeatedly. Typical conductance-distance traces were measured and given in Fig. S1a with a sampling rate of 20 *k*Hz under the bias of 100 mV. Before the breakage of gold electrodes pair, there are distinct plateaus at integral multiples of G_0, while after the breakage of gold electrodes pair, there is a tunneling profile without any discernable plateau. Fig. S1b and Fig. S1c display the corresponding conductance histogram and 2D conductance-distance histogram constructed from ~400 traces without data selection, respectively. In the pure solvent without target molecules, we got the stretching curves without any plateaus, suggesting the gold electrodes were clean for the single molecule conductance measurements. The stretching rate was calibrated using our previous reported methods.[1, 2] By applying the tunneling decay constant of $\log(G/G_0)/\ \Delta z = -5.5\ nm^{-1}$, we calibrated stretching rate to make the relative displacement (Δz) in the conductance region of $10^{-3.5}$ to $10^{-5.5}$ G_0 be ~0.36 nm (-2/-5.5 = ~0.36 nm), as shown in the inset of Figure S1(c).

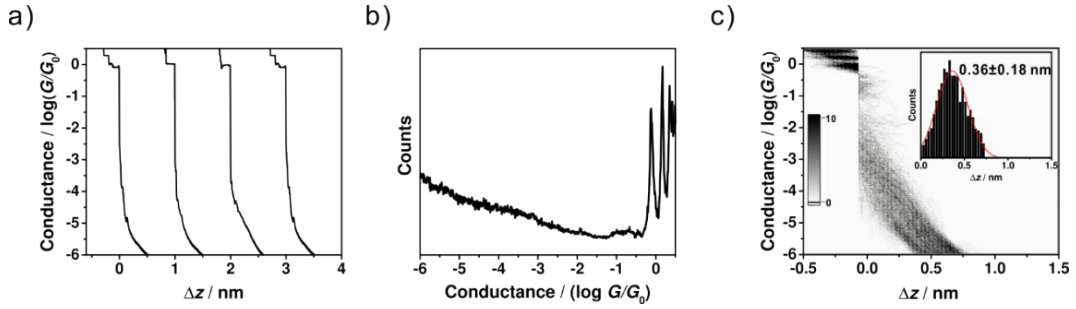

Fig. S1. (a) Typical conductance-distance traces of clean gold electrodes pair that recorded during the MCBJ opeartion. (b) Conductance histogram and (c) 2D conductance-distance histogram constructed from ~400 traces, respectively. Inset: the relative displacement distribution of the conductance region of $10^{-3.5}$ to $10^{-5.5}$ G_0.

2. Detailed distribution of the four types of traces.

To investigate the distribution of the four types of traces, we had to define the four types explicitly and quantitatively. First, as shown in Fig. S2a, the peaks of high conductance and low conductance were fitted, and we defined $10^{-2.5}$ G_0 and $10^{-4.6}$ G_0 as the tails of the high conductance peak and low conductance peak, respectively. Thus, the high conductance regime was defined as the area between the points at which the conductance values are $10^{-2.5}$ G_0 and $10^{-0.3}$ G_0, while the low conductance regime was defined as the area between $10^{-4.6}$ G_0 and $10^{-2.5}$ G_0. For clarity, in Fig. S2a the high conductance and low conductance regimes were highlighted by dashed frame. Second, we statistically analyzed the distributions of the plateau lengths within the high conductance and low conductance regimes. As illustrated in Fig. S2b and Fig. S2c, we found that the plateau length for high conductance regime is in between [0.07, 0.71], while for low conductance it is [0.15, 0.79]. On this basis, we classified the traces to the four types by their plateau lengths at high conductance and low conductance regimes. Particularly, with respect to an individual trace, only if the length of its fragment within the high conductance regime is in between [0.07, 0.71], it was identified that there is a high conductance plateau in this trace. This rule was also applied to identify the low conductance plateau.

Table S1 gives the detailed rules for the identification of high conductance and low conductance plateau, as well as the percentages of the four types of traces. In the main text, Fig. 1c gives the conductance histogram that constructed from all traces (blue), as well as the conditional histograms constructed from those traces with two conductance plateaus (purple), high conductance only (red), low conductance only (green) and no plateau (black), respectively.

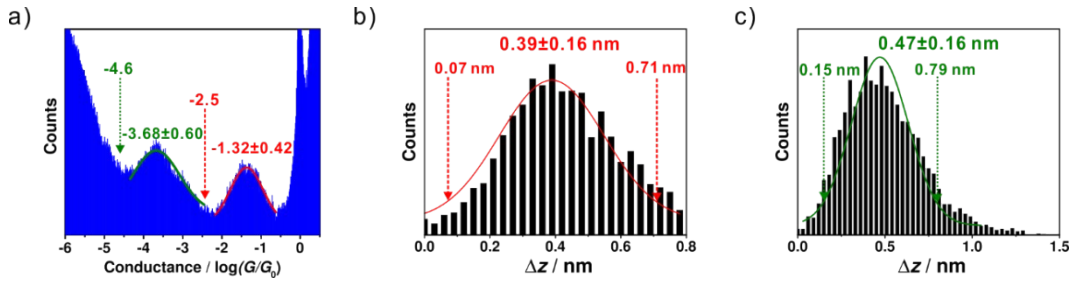

Fig. S2. (a) The fitted line for the peaks of high conductance and low conductance, where the tails for the two peaks were highlighted by arrows. (b) The fitted line for the distribution of the plateau lengths within the high conductance regime, where the interval adopted for the following identification of high conductance plateau was highlighted by red arrow. (c) The fitted line for the distribution of the plateau lengths within the low conductance regime, where the interval adopted for the following identification of high conductance plateau was highlighted by green arrow.

Table S1. Detailed rules for the identification of high conductance and low conductance plateaus, and the resulted percentages of the four types of traces.

	Plateau length within the high conductance regime	Plateau length within the low conductance regime	Number of traces	Percentage
Two plateaus	0.07~0.71	0.15~0.79	4508	95.51%
Only high conductance	0.07~0.71	0~0.15	134	2.84%
Only low conductance	0~0.07	0.15~0.79	67	1.42%
No plateau	0~0.07	0~0.15	11	0.23%
All	0~0.71	0~0.79	4720	100%

3. Approximation of the length of dimeric-BDT.

Density functional theory (DFT) calculation were performed with B3LYP functional, Gaussian basis (6-311G**), as implemented in Gaussian09 package.[3] Fig. S3 gives the schematic representation of an optimized **dimeric-BDT** molecule anchored between gold atoms. From this equilibrium structure, the dihedral angle along S-S axis (C1-S1-S2-C2) is measured to be 81.6°. This value agrees well with the experimental result that reported previously.[4, 5] Then we constrained the angle at anchoring S atoms (Au1-S3-C3 and Au2-S4-C4) to be 180°, and the distance Au1-Au2 is measured to be 13.16 Å.

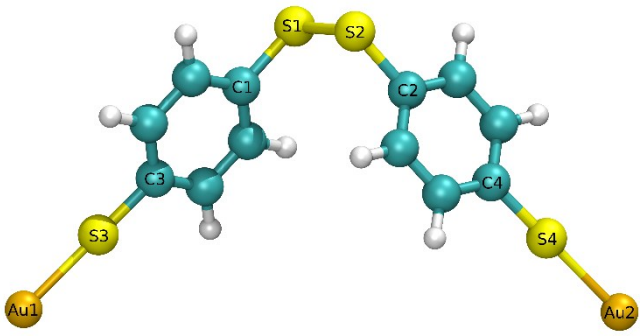

Fig. S3. The schematic representation of an optimized Au/**dimeric-BDT**/Au single-molecule junction.

4. Photographs of our homebuilt MCBJ-SERS setup.

In-situ SERS characterization was performed in Renishaw InVia system under 50X-long working distance objective lens (NA 0.55), with an excitation wavelength 785 nm and all spectra were collected with the same exposure time for 10 s under the same power density of ~0.35 mW/μm^2.

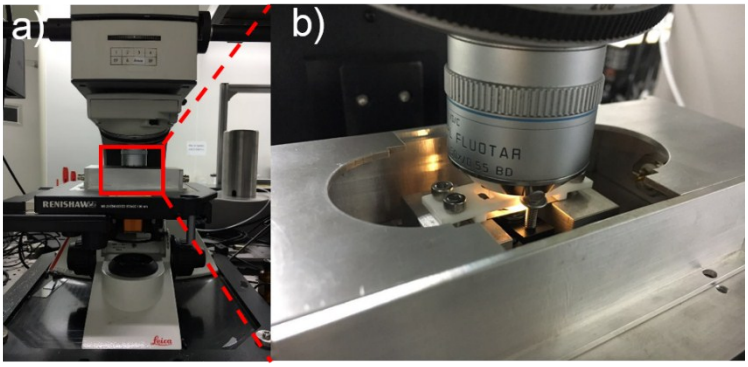

Fig. S4. Photographs of our homebuilt MCBJ-SERS setup.

5. Comparison of the Raman shifts of the υ_1 and υ_{8a} modes.

We observed that the MCBJ-SERS spectra experienced red-shifts compared to the spectrum from the bulk powder of BDT. The vibration modes of ring breathing modes (1075 cm^{-1}, υ_1) and C=C stretching mode (1579 cm^{-1}, υ_{8a}) were red-shifted to 1064 and 1569 cm^{-1}. The charge transfer at the Au/molecule interfaces weakened the intramolecular bonds, reducing the energy of the vibration modes. Thus, the shifted features can be seen as the signature of Au/BDT/Au junction formation.

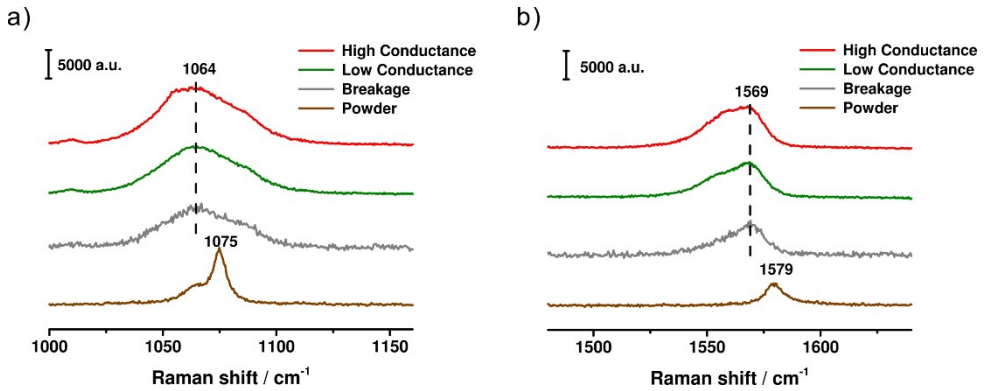

Fig. S5. The Raman shift of the (a) υ_1 and (b) υ_{8a} modes, respectively. SERS spectra were collected when the molecular junction was mechanically controlled at the regimes of high conductance (red), low conductance (green), and breakage (gray), respectively. Compared to the ordinary Raman spectrum of **BDT** powder (brown), a distinct red shift was observed in these three spectra. Laser excitation: 785 nm.

6. Comparison of the S-S bond intensity in SERS before and after addition the inhibitor into BDT.

We collected SERS spectra of **BDT** and **BDT** with the S-S bond inhibitor TCEP (Fig. S6a). After the intensity normalization, the characteristic peak of S-S bond at 485 cm^{-1} was weaken after the addition of TCEP, which can further reveal that the formation of disulfide bond will be restrained in such inhibitor. Together with the observation that the low conductance peak became inconspicuous with the existence of TCEP in the controlled conductance measurements (Fig. 4a and Fig 4b), it can be inferred that such low conductance feature attributed to the formation of the **dimeric-BDT**, which can be restrained by the S-S bond inhibitor.

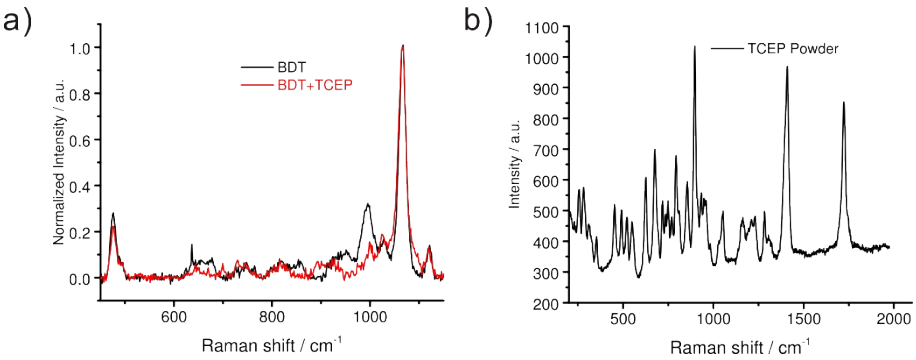

Fig. S6. (a) SERS spectra of **BDT** before (black) and after (red) the addition of TCEP. (b) The Raman spectrum of pure TCEP powder.

7. Low concentration conductance measurement of BDT.

We conducted the BDT conductance measurement under a lower concentration of a 10^{-4} mM **BDT** in a mixed ethanol (EtOH) and 1, 3, 5-trimethylbenzene (TMB) solvent (v : v=1 : 49), as shown in Fig. S7. A low conductance feature can be seen in Fig. S7a and S7b, which did not show a suppression of dimer formation. Since the oxidation of BDT to form dimer was inevitable in our testing environment, even trace dimer molecules in the solution can be detected.

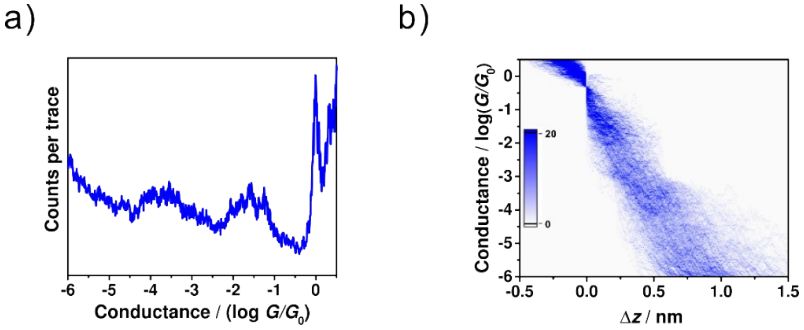

Fig. S7. (a) Conductance histogram and (b) 2D conductance-distance histogram constructed from 532 curves in 10^{-4} mM BDT solution.

8. Conductance measurements of pentane-1,5-dithiol (PDT).

To confirm that the low conductance was attributed to the S-S dimerization rather than π-π stacking of two adjacent molecules, we performed a supplementary experiment using pentane-1,5-dithiol (PDT) which has no π component. Two conductance peaks at $10^{-3.21}$ and $10^{-4.75}$ G_0 were observed in the 1D conductance histogram of Au/PDT/Au junction (Fig. S8a, blue lines). And in the 2D conductance-distance histogram (Fig. S8b), there are two intensified regimes, showing that two molecular configurations were formed during the MCBJ operation. The high conductance value was in agreement with the previous reported results.[6, 7] After adding TCEP as an inhibitor of the formation of S-S bond, the intensity of the high conductance peak remained unchanged (Fig. S8a). In contrary, the low conductance peak in the 1D conductance histogram (Fig. S8a), as well as the intensity cloud of the low conductance in the 2D conductance histogram (Fig. S8b and S8c), became inconspicuous, showing the same trend in the **BDT** junction.

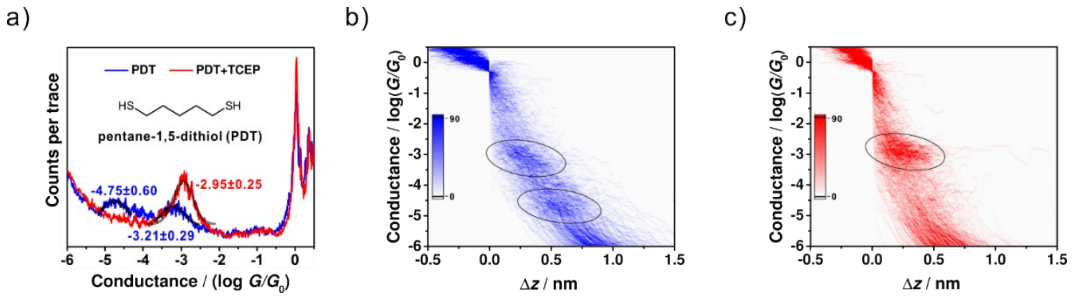

Fig. S8. (a) Conductance histogram of PDT before (blue) and after (red) the addition of TCEP. 2D conductance-distance histogram of PDT (b) and after the addition of TCEP (c).

References

1. W. Hong, D. Z. Manrique, P. Moreno-García, M. Gulcur, A. Mishchenko, C. J. Lambert, M. R. Bryce and T. Wandlowski, *J. Am. Chem. Soc.*, 2012, **134**, 2292-2304.
2. W. Hong, H. Valkenier, G. Mészáros, D. Z. Manrique, A. Mishchenko, A. Putz, P. M. García, C. J. Lambert, J. C. Hummelen and T. Wandlowski, *Beilstein J. Nanotechnol.*, 2011, **2**, 699.
3. M. J. Frisch, G. W. Trucks, H. B. Schlegel, G. E. Scuseria, M. A. Robb, J. R. Cheeseman, G. Scalmani, V. Barone, B. Mennucci, G. A. Petersson, H. Nakatsuji, M. Caricato, X. Li, H. P. Hratchian, A. F. Izmaylov, J. Bloino, G. Zheng, J. L. Sonnenberg, M. Hada, M. Ehara, K. Toyota, R. Fukuda, J. Hasegawa, M. Ishida, T. Nakajima, Y. Honda, O. Kitao, H. Nakai, T. Vreven, J. A. Montgomery, Jr., J. E. Peralta, F. Ogliaro, M. Bearpark, J. J. Heyd, E. Brothers, K. N. Kudin, V. N. Staroverov, R. Kobayashi, J. Normand, K. Raghavachari, A. Rendell, J. C. Burant, S. S. Iyengar, J. Tomasi, M. Cossi, N. Rega, J. M. Millam, M. Klene, J. E. Knox, J. B. Cross, V. Bakken, C. Adamo, J. Jaramillo, R. Gomperts, R. E. Stratmann, O. Yazyev, A. J. Austin, R. Cammi, C. Pomelli, J. W. Ochterski, R. L. Martin, K. Morokuma, V. G. Zakrzewski, G. A. Voth, P. Salvador, J. J. Dannenberg, S. Dapprich, A. D. Daniels, Farkas, J. B. Foresman, J. V. Ortiz, J. Cioslowski and D. J. Fox, *Gaussian 09 Revision B.01*, Gaussian, Inc., Wallingford CT, 2010.
4. J. S. Ricci and I. Bernal, *J. Am. Chem. Soc.*, 1969, **91**, 4078-4082.
5. A. Modelli and D. Jones, *J. Phys. Chem. A*, 2006, **110**, 10219-10224.
6. C. R. Arroyo, E. Leary, A. Castellanos-Gómez, G. Rubio-Bollinger, M. T. Gonzalez and N. Agraït, *J. Am. Chem. Soc.*, 2011, **133**, 14313-14319.
7. E. Wierzbinski, X. Yin, K. Werling and D. H. Waldeck, *J. Phys. Chem. B*, 2012, **117**, 4431-4441.